# Microscopic origin of U_{A}(1) symmetry violation in the high temperature phase of QCD

Viktor Dick, Frithjof Karsch, Edwin Laermann, Swagato Mukherjee, and Sayantan Sharma

# Microscopic Origin of $U_A(1)$ Symmetry Violation in the High Temperature Phase of QCD

Viktor Dick,[1] Frithjof Karsch,[1, 2] Edwin Laermann,[1] Swagato Mukherjee,[2] and Sayantan Sharma[2]

[1]*Fakultät für Physik, Universität Bielefeld, D-33615 Bielefeld, Germany*
[2]*Brookhaven National Laboratory, Upton, NY 11973, USA*

We investigate the low-lying eigenmodes of the Dirac matrix with the aim to gain more insight into the temperature dependence of the anomalous $U_A(1)$ symmetry. We use the overlap operator to probe dynamical QCD configurations generated with (2+1)-flavors of highly improved staggered quarks. We find no evidence of a gap opening up in the infrared region of the eigenvalue spectrum even at $1.5\,T_c$, $T_c$ being the chiral crossover temperature. Instead, we observe an accumulation of near-zero eigenmodes. We argue that these near-zero eigenmodes are primarily responsible for the anomalous breaking of the axial symmetry still being effective. At $1.5\,T_c$, these near-zero eigenmodes remain localized and their distribution is consistent with the dilute instanton gas picture. At this temperature, the average size of the instantons is $0.223(8)\,\mathrm{fm}$ and their density is $0.147(7)\,\mathrm{fm}^{-4}$.

## I. INTRODUCTION

Owing to the near-degeneracy and smallness of the up and down quark masses, the Quantum Chromo-dynamics (QCD) Lagrangian possesses an approximate $U_L(2) \times U_R(2) \equiv SU_L(2) \times SU_R(2) \times U_V(1) \times U_A(1)$ symmetry. The fact that we do not see parity doublet hadrons in our world implies that the $SU_L(2) \times SU_R(2)$ chiral symmetry is spontaneously broken down to the $SU_V(2)$ isospin symmetry of the vacuum. It is well known from first principle lattice QCD studies that above the chiral crossover [1–4] temperature of $T_c = 154(9)\,\mathrm{MeV}$ [5] the chiral symmetry of QCD gets restored.

On the other hand, the axial $U_A(1)$ symmetry of the QCD Lagrangian is always broken due to the presence of quantum fluctuations. This gives rise to the well-known anomalous non-conservation of the axial current [6, 7]. The explicit violation of the global $U_A(1)$ symmetry is due to the presence of topologically nontrivial gauge field configurations [8]. Although $U_A(1)$ is not an exact symmetry of QCD, the magnitude of its breaking near $T_c$ is expected to influence the nature of the chiral phase transition in the limit of two vanishingly small light quark masses. Perturbative renormalization group studies of model quantum field theories with the same global symmetries as QCD suggest that if $U_A(1)$ is not effectively restored at $T_c$, the chiral phase transition is of second order, belonging to the 3-dimensional $O(4)$ universality class [9–14]. If the axial symmetry gets effectively restored for $T \sim T_c$, the chiral phase transition can be either of first order [9, 10] or of second order with the symmetry breaking pattern $U_L(2) \times U_R(2) \to U_V(2)$ [11, 12]. In order to resolve the nature of the phase transition of QCD with two light quark flavors it is thus important to understand the significance of the anomalous $U_A(1)$ in the high temperature phase.

At low temperatures, $U_A(1)$ is also broken explicitly by the presence of a non vanishing vacuum chiral condensate. In the chirally symmetric phase, the vacuum condensate vanishes and the mechanism of global $U_A(1)$ breaking can be studied directly. The microscopic mechanism for $U_A(1)$ breaking in the chirally symmetric phase of QCD presents an intriguing puzzle. The chiral condensate, which is the order parameter related to the restoration of chiral symmetry in QCD with massless quarks, can be expressed in terms of the eigenvalues $\lambda$ of the Dirac operator as

$$\langle \bar{\psi}\psi \rangle \overset{V \to \infty}{\Rightarrow} \int_0^\infty \mathrm{d}\lambda \frac{2m\,\rho(\lambda, m)}{\lambda^2 + m^2} \,, \tag{1}$$

where $\rho(\lambda, m)$ is the eigenvalue density. On the other hand, $U_A(1)$ is not a global symmetry, so one cannot define a corresponding order parameter. For two light quark flavors, an approximate restoration of $U_A(1)$ would result in the degeneracy of the correlation functions of the pion and the scalar iso-triplet delta meson [15]. Specifically, the difference of the integrated correlation functions of these mesons in terms of the eigenvalues of the Dirac operator is

$$\chi_\pi - \chi_\delta = \int \mathrm{d}^4 x \ \left[ \langle i\pi^+(x) i\pi^-(0) \rangle - \langle \delta^+(x)\delta^-(0) \rangle \right]$$
$$\overset{V \to \infty}{\Rightarrow} \int_0^\infty \mathrm{d}\lambda \frac{4m^2\,\rho(\lambda, m)}{(\lambda^2 + m^2)^2} \,. \tag{2}$$

In the limit of vanishingly small quark mass $m$ and infinite volume $V$, the chiral condensate is proportional to the density of near-zero eigenvalues in accordance with the Banks-Casher relation [16], $\langle \bar{\psi}\psi \rangle = \pi\rho(0, 0)$. For $T \gtrsim T_c$, chiral symmetry gets restored and the chiral order parameter $\langle \bar{\psi}\psi \rangle$ vanishes implying that $\rho(0, 0)$ must also vanish. Motivated by the free theory limit at finite temperature, where the spectral density $\rho(\lambda, 0)$ has a gap up to the lowest fermion Matsubara frequency, $0 \leq \lambda < \pi T$, one possibility by which chiral symmetry restoration may occur in the chiral limit is through the generation of a gap in the infrared part of the eigenvalue spectrum. Such a scenario, however, would also lead to

the vanishing of $\chi_\pi - \chi_\delta$, i.e. to the effective restoration of both chiral and $U_A(1)$ symmetry.

In fact, more rigorous calculations based on chiral Ward identities for up to 4-point correlation functions show [17] that if the eigenvalue density for QCD with two light quark flavors is an analytic function in $m^2$, it must have the form $\lim_{m\to 0} \rho(\lambda, m) \sim \lambda^3 + \mathcal{O}(\lambda^4)$ in the chirally symmetric phase, similar to that for the free theory at $T = 0$. It was further shown [17] that, in this case all correlation functions up to 6-point which are related through $U_A(1)$ symmetry will be degenerate, making the anomalous breaking of $U_A(1)$ invisible in these correlation functions. Thus, if $U_A(1)$ breaking is finite through the nondegeneracy of the 2-point correlation functions such as $\chi_\pi - \chi_\delta$, the eigenvalue density must be nonanalytic in $m^2$. Two such possible forms of the infrared eigenvalue spectrum, compatible with $\langle \bar{\psi}\psi \rangle = 0$ but $\chi_\pi - \chi_\delta \neq 0$ for $m \to 0$, have been speculated in [18], namely $\rho(\lambda, m) \sim m^2 \delta(\lambda)$ and $\rho(\lambda, m) \sim |m|$. The functional form of the infrared eigenvalue density in the chirally symmetric phase of QCD remains an open and interesting theoretical question.

The global $U_A(1)$ breaking at $T = 0$ is intimately connected to the presence of topologically nontrivial configurations of the QCD gauge fields [8]. It is well known that localized topological structures like instantons give rise to zero modes of the Dirac operator and the corresponding wavefunctions remain localized [19]. The occurrence of near-zero modes can possibly also be traced back to the underlying topology of the gauge field configurations. For example, the particular form of the eigenvalue density of the Dirac operator $\rho(\lambda, m) \sim m^2 \delta(\lambda)$ in the infrared can be motivated from the fact that a small shift from zero of the near-zero modes resulting from the weak interactions among widely separated instantons and antiinstantons can be neglected, leading to a $\delta(\lambda)$ behavior. The $m^2$ factor naturally arises from the two light fermion determinants. At high enough temperatures, it has been shown that the dilute gas of instantons is a reasonable description of pure gauge theory [20, 21]. Within this approximation the instanton density is suppressed with decreasing value of the gauge coupling and eventually vanishes when $T \to \infty$ [20]. This dilute gas model is expected to be a good description of the high temperature phase of QCD as well [20]. The $U_A(1)$ breaking can be explained within such a model only for small enough values of the gauge coupling, i.e. at sufficiently high temperature and for small sizes of the instantons. It is however unclear whether such a mechanism can explain the $U_A(1)$ breaking for the more relevant temperature range from $T_c$ to a few times $T_c$. Near $T_c$ the instantons and antiinstantons may not be widely separated and weakly interacting, as described by the Instanton Liquid Model (ILM) [22]. In this model, chiral symmetry breaking arises due to the fermion modes associated with strongly interacting and overlapping instantons. As the temperature is increased, it was proposed that there is a transition from a liquid phase of disordered instantons and antiinstantons

to a phase of instanton-antiinstanton molecules [23, 24]. The chiral symmetry restoration at finite temperature may not necessarily be due to the suppression of the instantons [25] but rather due to the temperature dependence of the fermion determinant, which favors polarized instanton-antiinstanton molecules. Thus, it is entirely possible that for $T \lesssim T_c \lesssim 2\,T_c$ other nonperturbative mechanisms responsible for $U_A(1)$ breaking may generate an accumulation of near-zero modes leading to a more complex form of the infrared eigenvalue spectrum [26].

Since topological structures in QCD are inherently nonperturbative, lattice QCD techniques are ideally suited to address issues related to the $U_A(1)$. Anomalous $U_A(1)$ breaking at high temperature was studied on the lattice by looking at the nondegeneracy of the 2 point correlation functions $\chi_\pi - \chi_\delta$ using staggered fermion formulation, which preserves a remnant of the continuum chiral symmetry on the lattice, in [27]; more recently with an improved staggered fermion formulation in [28] and with $\mathcal{O}(a)$ improved Wilson fermions in [29]. In all the cases, it was observed that $U_A(1)$ was not effectively restored at $T \gtrsim T_c$. Recently, this issue was revisited in a study of the infrared eigenvalue spectrum of highly improved staggered quarks (HISQ) [30] and a similar conclusion was reached [31]. However, for staggered fermions the connection between topology and fermion zero modes and hence the reproduction of the index theorem is a very subtle issue [32]. Attempts to study this problem with fermions with exact chiral symmetry on the lattice have produced juxtaposing results. Studies with domain wall fermions [18, 33] but with a heavier than physical pion mass of 200 MeV support the scenario that $U_A(1)$ remains broken for $T \gtrsim T_c$. The eigenvalue density of the Dirac operator for $T \lesssim 1.2\,T_c$ has a small peak structure in the infrared favoring the form of $\rho(\lambda, m) \sim m^2 \delta(\lambda)$, which can largely account for the origin of the axial anomaly. However, even in these studies a clear separation of the zero and near-zero modes was not possible due to moderate residual chiral symmetry breaking effects induced by the mixing of the left and right handed fermions along the finite fifth dimension. On the other hand, another independent preliminary study with so-called optimal domain wall fermions and physical pion mass reports effective restoration of $U_A(1)$ above $T_c$ [34]. A study using overlap fermions restricted to the trivial topological sector of QCD on relatively small volumes also suggests that $U_A(1)$ is effectively restored at $T \sim T_c$ [35]. However, it is well known that simulations with fixed topology are more sensitive to finite volume effects and, at present, it is difficult to perform calculations with larger lattice volumes or for fluctuating topology in the case of overlap fermions due to prohibitively large computational costs. Recently reweighting domain wall fermion eigenspectrum to obtain effectively the eigenspectrum of the overlap fermions have been performed for small lattice volumes [36], which suggest effective restoration of $U_A(1)$ above $T_c$.

Measuring the underlying topology of the gauge fields

on the lattice requires careful analysis. The gauge fields are defined as links connecting the adjacent lattice sites, which can be continuously deformed to unity. To study localized topological structures one has to remove the ultraviolet fluctuations of the fields or approach successively to the minimum of the classical action. The latter is done by cooling the gauge configurations [37]. The ultraviolet fluctuations can be reduced using smearing [38], which involves replacing each gauge link by an average over the neighboring links. It is then possible to measure the topological charge on the lattice using the discretized version of the integrated $F\tilde{F}$ operator. The most popularly used smearing technique, known as the hypercubic (HYP) smearing [39], has been shown to provide a good estimate of the topological susceptibility. However, successive smearing may lead to small instantons being undetected and a change in the large scale structure of the gauge fields. Alternatively, one can make use of the index theorem [40], which relates the difference between the number of right and left-handed fermion zero modes to the topological charge of the gauge fields. The advantage of this method is that it naturally connects topological structures and the eigenmodes of the Dirac operator, which are global quantities and depend on the gauge links of the entire lattice.

In the present work we address the temperature dependence of $U_A(1)$ and probable microscopic mechanisms responsible for its breaking in the high temperature phase of QCD by studying the infrared eigenmodes of overlap fermions [43] on the background of dynamical (2+1) flavors of HISQ gauge field configurations with nearly physical fermion masses and large volumes. This HISQ discretization scheme has been used for extensive studies on QCD thermodynamics [5, 41] and has small discretization errors, resulting in the least taste symmetry breaking among all commonly used staggered fermion discretizations. Preliminary studies with HISQ fermions [42] also provide hints that in the continuum limit for two vanishingly small light quark masses, the QCD chiral transition may belong to the 3-dimensional $O(4)$ universality class. The issues about the lack of an index theorem of the HISQ is overcome by using the Overlap Dirac fermions to probe the topology of the HISQ gauge configurations. Overlap Dirac fermions circumvent the Nielsen-Ninomiya No-go theorem [44] by sacrificing the ultra-locality criterion, preserve an exact chiral symmetry [43] and an exact index theorem [45] and reproduce the correct anomaly [46] even at nonzero lattice spacing. Employing the index theorem for the overlap fermions, the topological structures in SU(2) [21] as well as SU(3) pure gauge theories [21, 47] have been studied earlier. However, the relationship between chiral and $U_A(1)$ symmetry also cannot be addressed within the framework of pure gauge theory and the presence of light dynamical fermions is necessary to address this question. Furthermore, it is a priori not evident whether the same dilute instanton gas picture also applies for QCD with near-physical, light dynamical fermions as the presence of light fermions would lead to interactions between instantons and induce anomaly effects.

This work is structured as follows: In Sec. II we provide all necessary computational details pertaining to this work. In III A we check the distribution of the topological charge measured by using the exact index theorem of overlap fermions. In III B we present and discuss our results on the eigenvalue distribution of overlap fermions on the dynamical HISQ configurations. The contribution of the low-lying eigenmodes towards $U_A(1)$ breaking is discussed in III C, while III D contains our results about the functional form of the eigenvalue density and its implications for $U_A(1)$ breaking. In III E we verify the robustness of the occurrence of near-zero modes. From III F to III G we discuss various different properties of the zero and near-zero eigenmodes. Finally, in IV we summarize and conclude this work. Preliminary results of this work were previously presented in [48].

## II. COMPUTATIONAL DETAILS

The set of $(2 + 1)$-flavor HISQ configurations used in this work was generated by the HotQCD collaboration [5]. Two lattice sizes were used in this study, $24^3 \times 6$ and $32^3 \times 8$. The strange quark mass $m_s$ is set to its physical value and the light quark mass in all these sets of configurations are chosen to be $m_l = m_s/20$, which corresponds to a Goldstone pion mass of $m_\pi = 160$ MeV in the continuum. We studied 5 sets of configurations, two at $T \sim T_c$, two at $T \sim 1.2\,T_c$ and one at $T \sim 1.5\,T_c$. Here, $T_c = 154(9)$ MeV [5] is the chiral crossover temperature in the continuum limit. Near $T_c$, in addition, we studied configurations generated by the Bielefeld-BNL collaboration [42] with lattice size $32^3 \times 6$ and a light quark mass of $m_l = m_s/40$, which corresponds to $m_\pi = 110$ MeV. This was to study whether the $U_A(1)$ breaking survives as the chiral limit is approached. We considered 90–160 configurations of each set, typically separated by 100 trajectories, and computed the eigenvalues of the overlap Dirac operator on them. The lattice sizes, strange to light quark mass ratio, temperatures and relevant statistics are shown in Tab. I.

| $N_\sigma^3 \times N_\tau$ | $m_l/m_s$ | $T$ [MeV] | $N$ | $N_\lambda$ |
|---|---|---|---|---|
| $24^3 \times 6$ | $1/20$ | 162.3 | 120 | 200 |
| $32^3 \times 6$ | $1/40$ | 162.3 | 90 | 400 |
| $32^3 \times 8$ | $1/20$ | 165.6 | 120 | 200 |
| $24^3 \times 6$ | $1/20$ | 199.0 | 100 | 100 |
| $32^3 \times 8$ | $1/20$ | 196.0 | 100 | 100 |
| $32^3 \times 8$ | $1/20$ | 237.1 | 160 | 50 |

Tab. I: Lattice size ($N_\sigma^3 \times N_\tau$), mass ratio ($m_l/m_s$), temperature ($T$), number of configurations ($N$) and number of eigenvalues that were computed per configuration ($N_\lambda$) for each ensemble.

We probe the low-lying eigenmodes of these HISQ gauge ensembles through the use of the massless overlap Dirac fermion operator

$$D_{\mathrm{ov}} = M \left[ 1 + \gamma_5 \mathrm{sgn} \left[ \gamma_5 D_W(-M) \right] \right] \; , \qquad (3)$$

where $D_W$ is the standard Wilson Dirac operator with the parameter $0 < M < 2$.

For the implementation of the sign function in the overlap operator, we computed the lowest 20 eigenvectors of $D_W^\dagger D_W$ using the Kalkreuter-Simma (KS) Ritz algorithm [49]. The sign function was computed for these low modes explicitly, while for the higher modes it was approximated by a Zolotarev rational function. The number of terms in the Zolotarev function was kept to be 15. The overlap operator satisfies the Ginsparg-Wilson(GW) relation with a deviation of no more than $10^{-7}$ at low temperatures and $10^{-10}$ at high temperatures. The square of the sign function deviated from identity by about $10^{-7}$–$10^{-9}$.

For each temperature, 50 lowest eigenvalues of $D_{\mathrm{ov}}^\dagger D_{\mathrm{ov}}$ were computed using the KS algorithm. The zero modes of $D_{\mathrm{ov}}^\dagger D_{\mathrm{ov}}$ come with chiralities $\pm 1$. The nonzero eigenvalues come in degenerate pairs with chiralities having opposite signs but equal magnitudes, which is usually different from unity. These features of the spectrum allow us to distinguish between the near and exact zero modes within a few iterations of the KS algorithm. The KS algorithm was run until the relative error on the nonzero eigenvalues of $D_{\mathrm{ov}}^\dagger D_{\mathrm{ov}}$ were estimated to be lower than $10^{-4}$ on average and the separation between zero and nonzero modes was clearly seen. In most cases, the number of eigenvalues was later increased by computing the eigenvalues of $P D_{\mathrm{ov}} P$, where $P$ is the projection to righthanded or lefthanded modes. This projected operator has the advantage that it only takes half the time to be applied and each nonzero eigenvector can be related to a pair of eigenvectors of $D_{\mathrm{ov}}^\dagger D_{\mathrm{ov}}$, further reducing computation time and memory requirement. However, the algorithm becomes quite unstable if the subspace that $P$ projects onto contains zero modes and can only be used on the opposite chiralities after identifying the zero modes.

For some applications, the eigenvectors of $D_{\mathrm{ov}}$ were required and not only those of $D_{\mathrm{ov}}^\dagger D_{\mathrm{ov}}$. Each degenerate pair of nonzero eigenvectors of the squared operator spans a two-dimensional space that also contains two eigenvectors of $D_{\mathrm{ov}}$, which are related to each other by an application of $\gamma_5$ and have eigenvalues that are complex conjugates of each other. These eigenvectors could be obtained by applying an appropriate unitary transformation to each of the original pairs.

We also checked the optimal value of the parameter $M$ used in the construction of the overlap operator. From partially quenched studies it is known that for certain choices of $M$, the corresponding $D_W^\dagger D_W$ can have very small eigenvalues, leading to the presence of spurious zero modes in the overlap operator [50]. We verified that for configurations without zero modes the choice of $M$ did

not affect the eigenvalues significantly within our precision. Moreover, for configurations with zero modes we chose $M$ such that the sign function and the GW relation were determined with highest accuracy, ensuring the best implementation of the overlap operator. Except for a few cases, especially near $T_c$, we chose $M = 1.8$.

For the $32^3 \times 6$ lattice with a light quark mass of $m_l = m_s/40$, the gauge configurations were rough and the convergence of the KS for $D_W^\dagger D_W$ was slow, leading to imprecise estimates of the GW relation and the sign function. In this case, we did two levels of HYP smearing to smoothen out the ultraviolet fluctuations. This enabled us to achieve a more precise estimation of the overlap sign function, similar to the precision achieved for the other ensembles. The effects of the smearing are further discussed in Section III E.

## III.  RESULTS

### A.  Topological charge distributions

The topological charge $Q$ was measured by counting the number of zero-modes of the overlap operator and determining their chiralities,

$$Q = n_+ - n_- \; , \qquad (4)$$

where $n_+$ ($n_-$) is the number of zero modes with chirality $+1$ ($-1$). Since the underlying HISQ gauge configurations were generated at zero strong CP violating angle $\theta$, at any temperature all the topological sectors should be spanned. However, the configurations may have been trapped in one topological sector and the autocorrelation times in such cases may be large. To avoid autocorrelation effects we usually chose the configurations to be separated by 100 Rational Hybrid Monte-Carlo trajectories. The time histories of the topological charge are shown in Fig. 1. It is evident that the autocorrelation effects are under control. The distribution is ergodic enough and on average $\langle Q \rangle \simeq 0$, for all temperatures. This gives us confidence that the statistics is sufficient in our present study. Moreover, we also observe many configurations with $|Q| \geq 1$ in all studied ensembles. In fact, even at $1.5\,T_c$ more than a third of the total number of configurations have $|Q| = 1$, confirming the importance of the $Q \neq 0$ configurations.

### B.  Eigenvalue spectra

In this section we show the eigenvalue density of the overlap operator at three temperatures – near $T_c$, at $1.2\,T_c$ and at a yet higher temperature of $1.5\,T_c$. The overlap fermion matrix in Eq. (3) is a normal matrix. In the complex plane, its dimensionless eigenvalues, $\tilde{\lambda}$, lie on a circle centered at $M$ and with a radius $M$, obeying $|\tilde{\lambda} - M|^2 = M^2$. The eigenvalues measured in our study
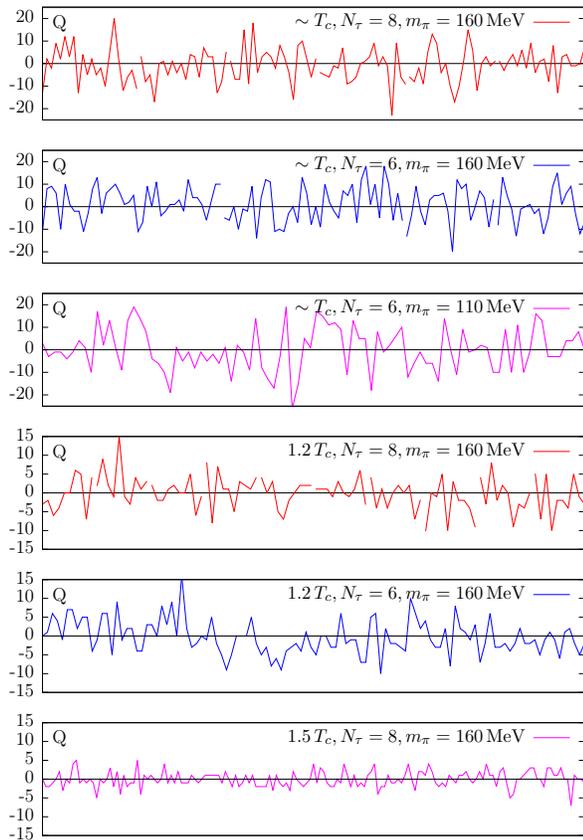
Fig. 1: Time histories of the topological charge, calculated from the zero modes of the overlap Dirac operator, for the HISQ configurations at $T \sim T_c$, $T \sim 1.2\,T_c$ and $T \sim 1.5\,T_c$. Configurations belonging to the same production stream are connected with lines.



Fig. 2: The eigenvalue density of the overlap operator on $32^3 \times 8$, $24^3 \times 6$ and $32^3 \times 6$ HISQ configurations near $T_c$. Only nonzero modes are included. The vertical line denotes the range of validity due to the finite number of computed eigenvalues.

lie on the circle very close to the origin with a very small real part. Hence, we always plot the eigenvalue density as a function of $\lambda$, where $a\lambda = \mathrm{Im}\tilde{\lambda}$. On the lattice, the eigenvalue density is defined as

$$a^3 \rho(\lambda) = \frac{1}{N_\sigma^3 N_\tau} \sum_i \delta\left(a\lambda - a\lambda_i\right), \qquad (5)$$

where the sum only includes values on the left part of the semicircle with $\mathrm{Re}\tilde{\lambda} < M$, and excludes values near $\tilde{\lambda} = 2M$ even though their imaginary part would also be small.

The eigenvalue distribution at three different temperatures is shown in Figs. 2, 3 and 4. The spectrum is truncated at some large eigenvalue since we measure only a finite number of them. We indicate the point beyond which the spectrum is not trustworthy anymore by a vertical line in red in each of the plots. It is estimated by first taking the highest computed eigenvalue of each configuration and then taking the minimum of these values over all the analyzed configurations.

As we emphasized earlier, the KS algorithm allowed us

to distinguish the zero modes from the near-zero modes using the chirality properties of the corresponding eigenvectors. In general, the eigenvalue distribution has three distinct features – the zero mode peak, a near-zero mode accumulation and the bulk eigenvalue region. The low-mode structure seen in the overlap eigenvalue spectrum is more pronounced than what has been found in the HISQ eigenvalue spectrum calculated on similar lattice volumes [31]. This may be due to the fact that for the staggered fermion operator the index theorem is very subtle. The differences are expected to disappear in the continuum limit which needs to be checked in future work. Near $T_c$, the first bin contains a large contribution from

zero modes which are omitted in Fig. 2 to focus on the infrared physics of only the near-zero eigenvalues. At this temperature, we do not observe any gap in the infrared part of the eigenvalue spectrum. The near-zero modes and the bulk modes appear to overlap significantly and the near-zero modes tend to develop a peak towards the infrared region. This peak becomes sharper as the light sea quark mass is lowered from $m_l = m_s/20$ to $m_l = m_s/40$ at fixed lattice spacing $1/6T$. The lattice volume has been increased as one goes from $m_l = m_s/20$ to $m_s/40$ such that $Lm_\pi$ is kept fixed. At $m_l = m_s/20$, the aspect ratio is $N_s/N_\tau = 4$, which is sufficient for calculating many thermodynamic quantities close to thermodynamic limit. However at present, no systematic analysis of the volume effects on eigenvalue spectrum has been performed. We cannot explicitly distinguish the finite volume effect from the chiral effect in shaping the near-zero peak. The near-zero peak also becomes sharper when we go to a finer lattice, from $N_\tau = 6$ to $N_\tau = 8$ at a fixed pion mass of $160\,\mathrm{MeV}$. This trend suggests that the near-zero mode accumulations will remain as the chiral and the continuum limits are approached.

At temperatures $1.2\,T_c$ and $1.5\,T_c$, both the zero modes denoted by the red bar and the near-zero and bulk modes are shown in Fig. 3 and Fig. 4. The separation between the near-zero mode accumulation and the bulk eigenvalue region becomes even more evident with increasing temperature. At $1.2\,T_c$, we study the eigenvalue spectrum at two different lattice spacings to estimate whether the infrared part of the spectrum is strongly affected by the lattice cutoff effects at higher temperatures. Keeping the physical bin size the same in units of $\lambda/T$ for comparison, we observe that the infrared region of the eigenvalue density remains practically unchanged when the lattice spacing goes from $1/6T$ to $1/8T$ at a fixed temperature $T$. This gives us confidence that the near-zero modes are not due to dislocations of the gauge fields. A more detailed study about the lattice artifacts is given in Sec. III D.

The number of zero and near-zero modes both decrease as the temperature is increased to $1.5\,T_c$ as shown in Fig. 4. There is a small peak of near-zero modes, while the number of bulk eigenvalues starts to rise very slowly and only gives a significant contribution beyond $\lambda_0 \simeq 0.4\,T$. This is reminiscent of some kind of band edge separating the two different regimes of eigenvalues, which is studied in detail in Sec. III G. Even at this temperature we do not observe a gap in the infrared sector of the eigenvalue spectrum. The presence of these near-zero modes is not due to the fact that we are also sampling configurations belonging to nonzero topological sectors in our study. This is evident from the lower panel of Fig. 4, where we show the eigenvalue distribution of only those configurations with topological charge $Q = 0$ at $1.5\,T_c$. The presence of near-zero modes is also observed for this particular subset of configurations.
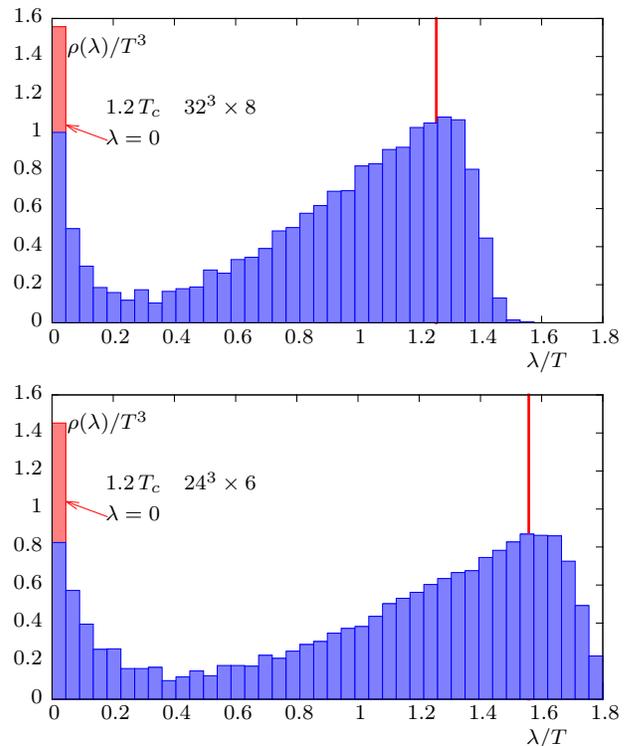


Fig. 3: The eigenvalue density for HISQ configurations using the overlap operator at $1.2\,T_c$. The lattice sizes are $32^3 \times 8$ and $24^3 \times 6$, respectively. The red line marks the range of validity.

## C. Near-zero eigenmodes and axial symmetry breaking

As introduced in Sec. I, $\omega \equiv \chi_\pi - \chi_\delta$ as defined in Eq. (2) is a measure that quantifies $U_A(1)$ breaking. Through a chiral Ward identity it can also be obtained

$$\omega = \frac{\langle \bar\psi\psi \rangle}{m} - \chi_{\mathrm{conn}} \qquad (6)$$

from the chiral condensate $\langle \bar\psi\psi \rangle = \frac{T}{V} \left\langle \mathrm{tr}\left(D_m^{-1}\partial_m D_m\right)\right\rangle$ and the connected chiral susceptibility $\chi_{\mathrm{conn}} = \frac{T}{V} \left\langle \partial_m \mathrm{tr}\left(D_m^{-1}\partial_m D_m\right)\right\rangle$, where $D_m = D_{\mathrm{ov}}(1 - am/2M) + am$ is the Dirac operator for overlap quarks with a (valence) quark mass $m$.

Thus, in terms of the eigenvalues of the overlap operator

$$a^2\omega = \frac{1}{N_\sigma^3 N_\tau} \left[ \frac{\langle |Q| \rangle}{(am)^2} \right. \qquad (7)$$
$$\left. + \left\langle \sum_{\tilde\lambda \neq 0} \frac{2(am)^2(4M^2 - |\tilde\lambda|^2)^2}{\left[|\tilde\lambda|^2(4M^2 - (am)^2) + 4(am)^2 M^2\right]^2} \right\rangle \right].$$

The first term is the contribution from the zero modes which vanishes in the thermodynamic limit.
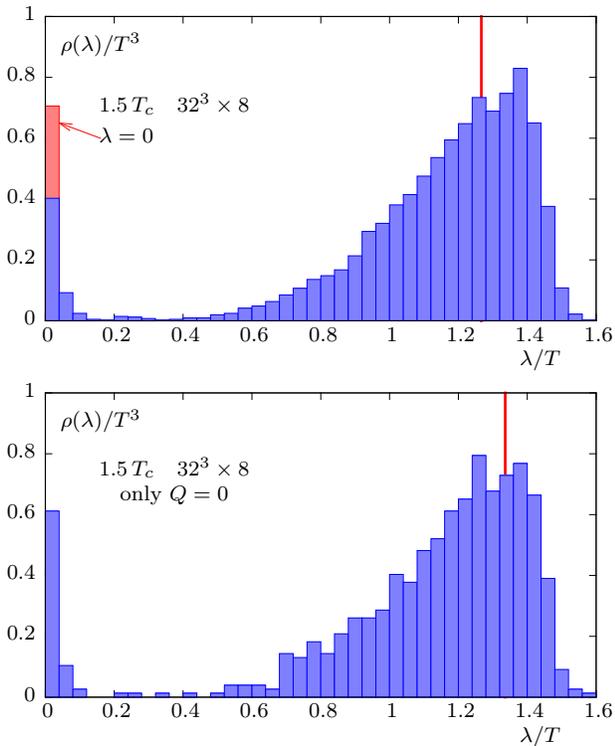
Fig. 4: The eigenvalue density for $32^3 \times 8$ HISQ configurations using the overlap operator for $1.5\,T_c$ for all values of $Q$ and also separately for the $Q = 0$ sector. The red line marks the range of validity.



Fig. 5: The tuning of the strange valence quark mass for overlap fermions on $N_\tau = 6$ (blue) and $N_\tau = 8$ (red) lattices near $T_c$. The horizontal lines mark the results for $m_s^2\omega_s/T^4$ (cf. Eq. (6)) independently obtained for the HISQ sea fermions. Filled (empty) points denote the overlap result with (without) the zero mode contribution.

Thus, having determined the low-lying eigenvalues of the overlap operator, $\omega$ can be computed from them. However, to explore the physics of the underlying HISQ configurations the overlap valence quark mass that enters Eq. (7) has to be tuned against some physical quantity measured on the same gauge configurations. In the present work we adopt a very simple strategy: we roughly tune the strange valence quark mass, $m_s$, and then study $\omega$ as a function of the light valence quark mass within a range of $m_l = m_s/20$ to $m_l = m_s/2$. To tune the strange valence quark mass we use the renormalized difference of the pseudo-scalar ($\eta_{s\bar{s}}$) and the (connected) scalar susceptibilities in the strange quark sector, $m_s^2\omega_s/T^4$. We calculated this renormalized quantity using strange valence overlap fermions and matched it with the same quantity calculated independently for the strange HISQ sea quarks. For the overlap fermions this quantity was estimated in two parts. We first calculated this quantity from the predetermined low-lying eigenvalues using Eq. (7), and then added the contribution of higher eigenvalues by performing inversions on the eigenspace orthogonal to the low-lying eigenmodes using random source vectors. The result of the strange valence quark mass tuning near $T_c$ is shown in Fig. 5. In order to monitor finite volume effects, we considered the exact zero modes separately and do not observe a significant contribution

from them to this quantity. The tuned masses obtained with and without the zero modes differ by about 5%.

In Fig. 6, we show a renormalized measure of $U_A(1)$ breaking, namely $m_l m_s \omega/T^4$, for a range of the light valence quark mass between $m_s/20$ and $m_s/2$. Assuming a Breit-Wigner distribution for the near-zero mode peak to model the $\delta(\lambda)$ like distribution discussed in the introduction, i.e. $\rho(\lambda)/T^3 = \rho_0 A/(A^2 + \lambda^2)$, the contributions of the near-zero modes in this renormalized measure of $U_A(1)$ breaking can be characterized as

$$\frac{m_l m_s}{T^4}\omega \propto \rho_0 m_s \frac{A + 2m_l}{(A + m_l)^2} \ . \tag{8}$$

In our partially quenched setup, where only the valence light quark mass $m_l$ is varied, this quantity has a finite value in the chiral limit $m_l \to 0$. In a full dynamical setup, its behavior will be governed by the dependence of $A$ and $\rho_0$ on the light sea quark mass. The simplest case of both $A$ and $\rho_0$ being proportional to the light sea quark mass, which is compatible with the trends discussed in Sec. III D, will also give a finite value and should be approximated in a partially quenched study. For light valence quark masses near to or smaller than the smallest near-zero eigenvalues, the computed quantity will approach zero, which is visible for the lowest masses near $T_c$. This is a finite volume effect in the sense that a larger volume will sample more eigenvalues in the near-zero mode region, which reduces the magnitude of the smallest eigenvalue and pushes this effect towards zero. Beyond that, we observe a smooth dependence on $m_l/m_s$ that is compatible with the Breit-Wigner ansatz and which is independent of the lattice spacing. It is also evident from Fig. 6 that the contribution of the near-zero modes to $\omega$ is substantially larger than that from the bulk modes. When going from $T \sim T_c$ to $T \sim 1.2\,T_c$, this quantity does not decrease significantly, supporting our conclusion that $U_A(1)$ is not effectively restored si-
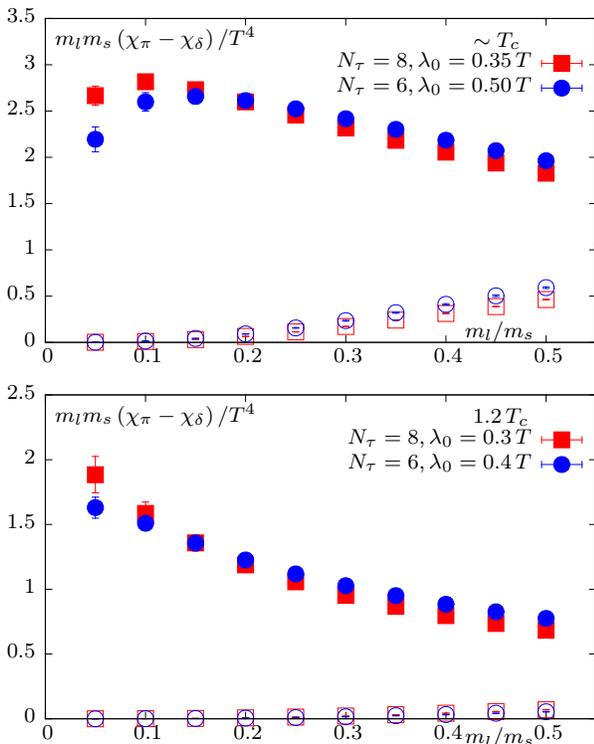
Fig. 6: A renormalized measure of $U_A(1)$ breaking for a range of valence light quark masses, $m_s/20 \leq m_l \leq m_s/2$ for ensembles with different $N_\tau$ at $T \sim T_c$ and $T \sim 1.2\,T_c$. The filled points denote the contribution from near-zero modes ($\lambda < \lambda_0$), while the empty points were calculated only from the bulk modes ($\lambda > \lambda_0$).

multaneously with the chiral symmetry.

### D. The functional form of the eigenspectra

In order to understand the general functional form of the eigenvalue density and in particular the near-zero region, we make a fit ansatz consisting of a Breit-Wigner peak for the near-zero modes and a polynomial behavior for the bulk part of the spectrum of the form,

$$\frac{\rho(\lambda)}{T^3} = \frac{\rho_0 A}{A^2 + \lambda^2} + c\lambda^\alpha \ . \tag{9}$$

We address three issues in this section. Firstly, a general idea about the dependence of the near-zero mode peak on the sea quark mass is necessary to understand what happens in the chiral limit. Secondly, it is important to check the dependence of the near-zero modes on the lattice cutoff to establish that these are physical and not mere lattice artifacts. Finally, the leading exponent that characterizes the rise of the bulk also provides information regarding the restoration of $U_A(1)$, hence its dependence on the temperature and lattice cutoff needs to be studied.
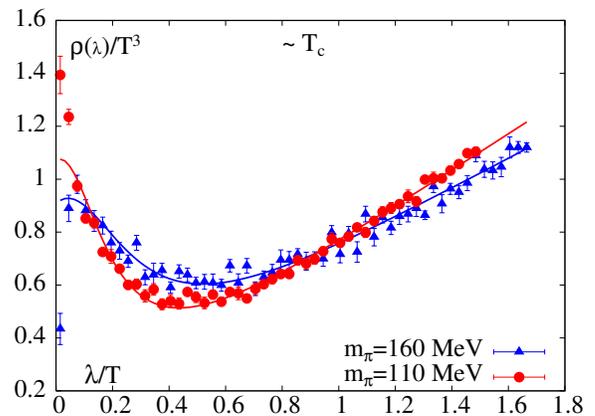


Fig. 7: Eigenvalue distribution at $T \sim T_c$ for $N_\tau = 6$ and two different sea quark masses compared to fits with Eq. (9).

The fit to the eigenvalue spectrum near $T_c$ for different sea quark masses is shown in Fig. 7. The error bars for each bin have been determined by a jackknife procedure over the set of gauge configurations. The parameter $A$, characterizing the width of the near-zero mode peak, falls from $0.35(4)\,T$ to $0.151(7)\,T$ when going from $m_l = m_s/20$ to $m_s/40$ and the prefactor $\rho_0$, indirectly controlling the height of the peak, also goes down from $0.28(3)\,T$ to $0.191(7)\,T$. This generally supports the picture of a delta function like peak forming in the chiral limit, with a decreasing peak height. However, as far as one can tell from two data points, the dependence of $\rho_0$ does not seem to be quadratic in the light sea quark mass near $T_c$, arguing against the dilute instanton gas picture as a good description of QCD at this temperature.

To examine cutoff effects one needs to compare a renormalized version of the eigenvalue density at different lattice spacings. One way to renormalize the eigenvalues is to scale them by the previously tuned strange quark mass. The corresponding renormalized eigenvalue density is then $m_s\rho(\lambda)$ since it leaves the quantity $m_s\langle\bar{\psi}\psi\rangle$ unchanged under renormalization. We therefore take the same ansatz as in Eq. (9) with $\lambda \to \lambda/m_s$ and the density replaced by its renormalized definition $m_s\rho(\lambda)/T^4$. Fits to the renormalized spectrum in dimensionless units at two different temperatures, $T_c$ and $1.2\,T_c$, are shown in Fig. 8. Taking a closer look at the near-zero mode peak, it is evident that the accumulation of near-zero modes is almost independent of the lattice spacing and is unlikely to be just a lattice artifact.

Finally, we discuss the exponent $\alpha$ of the characteristic $\lambda^\alpha$ rise of the bulk eigenvalues. As mentioned in Sec. I, under the assumption of analyticity of the eigenvalue density in $m^2$, detailed analytical calculations based on up to 4-point chiral Ward identities show [17] that in the chiral symmetric phase of QCD the leading $\lambda$ dependence should be similar to that for the free theory, i.e. $\lim_{m\to 0}\rho(\lambda, m) \sim \lambda^3$. In such a case, the effect of $U_A(1)$

Fig. 9: Eigenvalue distribution at $1.5\,T_c$ together with $a\,(\lambda - \lambda_0)^\alpha$ fit to the bulk eigenmodes.

Fig. 8: The renormalized eigenvalue spectra near $T_c$ (top) and at $1.2\,T_c$ (bottom), both for two different lattice spacings. The lines indicate fits to Eq. (9) with $\lambda \to \lambda/m_s$ and $\rho(\lambda)/T^3 \to m_s\rho(\lambda)/T^4$.

breaking should be invisible in at least up to 6-point correlation functions. In light of this, it is interesting to characterize the rise of the bulk eigenvalues. As shown in Fig. 7, near $T_c$ the rise of the bulk eigenvalues for our two $N_\tau = 6$ lattices with quark masses $m_l = m_s/20$ and $m_l = m_s/40$ is described by the exponents $\alpha = 0.92(5)$ and $\alpha = 0.98(4)$, respectively. A fit to the renormalized eigenvalue spectrum near $T_c$ further yields $0.86(2)$ for $N_\tau = 8$, see Fig. 8. Thus, near $T_c$ a linear rise of bulk eigenvalues is favored for both lattice spacings and quark masses. Interestingly, chiral perturbation theory [51] and the ILM [52] show that a contribution to $\rho(\lambda)$ linear in $\lambda$, which results in a non vanishing connected susceptibility $\chi_{\rm conn}$, is absent for two light flavors and only present for $N_f > 2$. On the other hand, for staggered fermions away from the continuum limit, taste violations lead to $\chi_{\rm conn} \neq 0$ also for $N_f = 2$ [53].

At $1.2\,T_c$ the rise of the bulk eigenvalues has a different exponent. From Fig. 8 it is evident that $\alpha \simeq 2$, independent of the lattice spacing. Note that a bulk eigenvalue density rising quadratically with $\lambda$ does not contribute to $\omega$. A similar linear behavior for $T \sim T_c$ and a quadratic rise for $T \sim 1.2\,T_c$ of the bulk eigenvalues was also ob-

served in the previous study with domain wall fermions [33] with a heavier pion mass, corroborating that the bulk rise is independent of the sea quark mass. On the other hand, the characteristic free theory like cubic rise of the bulk eigenvalue density was only observed at $1.5\,T_c$ as shown in Fig. 9. At $1.5\,T_c$, the near-zero mode peak reduces significantly and the separation between the bulk and the near-zero modes is distinctly visible. Our fit ansatz for the bulk is modified accordingly as $(\lambda - \lambda_0)^\alpha$ to represent this feature, which gives a smaller $\chi^2$ per degrees of freedom than the original ansatz in Eq. (9). The parameter $\alpha$ and the goodness of fit at different temperatures are compiled in Tab. II.

| $N_\sigma^3 \times N_\tau$ | $m_l/m_s$ | $T$ [MeV] | $\alpha$ | $\chi^2/$dof |
|---|---|---|---|---|
| $24^3 \times 6$ | $1/20$ | 162.3 | 0.92(5) | 1.32 |
| $32^3 \times 6$ | $1/40$ | 162.3 | 0.98(4) | 1.84 |
| $32^3 \times 8$ | $1/20$ | 165.6 | 0.86(2) | 0.92 |
| $24^3 \times 6$ | $1/20$ | 199.0 | 1.9(2) | 1.16 |
| $32^3 \times 8$ | $1/20$ | 196.0 | 1.9(1) | 1.21 |
| $32^3 \times 8$ | $1/20$ | 237.1 | 3.0(4) | 1.30 |

Tab. II: Lattice size ($N_\sigma^3 \times N_\tau$), mass ratio ($m_l/m_s$), temperature ($T$), the exponent $\alpha$ characterizing the $\lambda^\alpha$ rise of the bulk eigenvalues $\lambda$ and the goodness of the fits performed on the eigenvalue distribution.

### E.   Robustness of the zero and near-zero modes

Detecting topological objects with fermion zero modes has the advantage that by construction the zero modes depend on all the gauge links distributed on a lattice. Still, if the underlying gauge fields are not smooth enough, the method might be hampered by the presence of unphysical fermion modes localized on structures
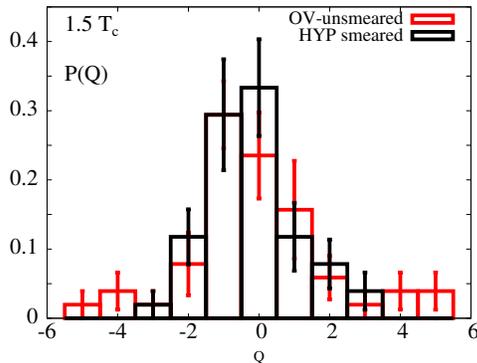
Fig. 10: The distribution of the topological charge, $Q$, at $1.5\,T_c$ for $32^3 \times 8$ HISQ configurations measured from the zero modes of the overlap operator and also from the gluonic operator $F\tilde{F}$ on the same gauge configurations after 10 levels of HYP smearing.



Fig. 11: The eigenvalue density at $1.5\,T_c$ and $N_\tau = 8$ before and after 10 steps of HYP smearing. The empty boxes are obtained when including zero modes and the dashed lines mark the ranges of validity.

called dislocations, which typically have a smaller classical action than instantons. These are lattice artifacts, i.e. effects of finite lattice spacing, and should disappear as the continuum limit is approached. It is therefore important to make sure that the observed infrared fermion modes are physical and do not solely arise as lattice artifacts. If the zero and near-zero eigenvalues are entirely due to the presence of dislocations, they are expected to disappear as the gauge fields are smoothed using smearing techniques. To check this we performed HYP smearing on the $32^3 \times 8$ configurations with $m_l/m_s = 1/20$ at $1.5\,T_c$.

Such smoothing methods are mandatory if one wants to compute the topological charge by means of a discretized version of its field theoretic definition

$$Q = \frac{1}{32\pi^2} \int \mathrm{d}^4 x F^a_{\mu\nu} \tilde{F}^a_{\mu\nu} \; . \tag{10}$$

The optimal number of smearing levels is usually chosen such that the topological charge measured this way on the smeared configurations has a value close to an integer. On our present lattices it turned out that 10 levels of HYP smearing were sufficient to give an integer value of the $F\tilde{F}$ operator summed over the whole lattice at $1.5\,T_c$. On all of these smoothed configurations we could verify that the value of $Q$ obtained from $F\tilde{F}$ matched exactly with the topological charge obtained by counting the zero modes of the overlap operator after smearing.

In Fig. 10, we compare the histogram for the topological charge measured by counting the fermion zero modes of unsmeared configurations with that measured using the purely gluonic observable $F\tilde{F}$ on the same configurations after smearing. Apparently, some zero modes disappear in the course of the smearing process; yet, the comparison indicates that the fermionic zero modes for these configurations do not arise only due to gauge field dislocations and are reflecting continuum physics.
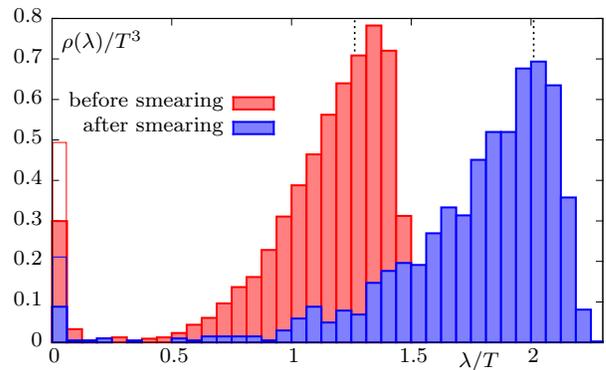
A similar behavior is observed for the near-zero modes. In Fig. 11, the comparison of the eigenvalue spectrum of the overlap operator on the original unsmeared configurations with the smeared ones reveals that the number of near-zero modes is somewhat reduced by smearing but that the near-zero mode accumulation is still present even after a substantial amount of smearing, indicating that these are not mere lattice artifacts like dislocations. We also found that the typical eigenvectors associated with the near-zero modes on a smeared configuration appear to be slightly less localized compared to the unsmeared case, suggesting that the reduction of the near-zero modes may be caused by the loss of small instantons due to smearing.

Finally, as already shown in Fig. 8, near $T_c$ as well as at $1.2\,T_c$ the comparison of the renormalized eigenvalue spectra at two different lattice spacings, $1/6T$ and $1/8T$, indicates that the near-zero mode accumulation remains nearly unchanged as the lattice spacing is reduced. One finally needs to perform continuum extrapolation of our results for the eigenvalue spectrum to understand whether the near-zero modes we observe are physical or are artifacts arising from our using the overlap operator to probe the configurations generated with HISQ action. It is assuring that we observe very little sensitivity of the near-zero modes to the change in lattice spacing at two different temperatures.

### F. Profiles of the zero and near-zero modes at high temperature

The fermion zero mode associated with an instanton is, at $T = 0$, localized in the region occupied by the instanton. At nonzero temperature however, the compactification of Euclidean time leads to periodic copies of instantons. Such classical finite action solutions of the gauge fields on the manifold $R^3 \times S^1$ are known as calorons.
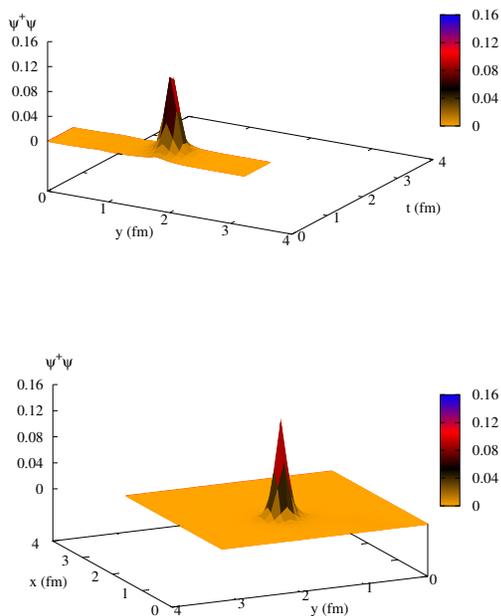
Fig. 12: Space-time profile of a zero mode at $1.5\,T_c$ for a typical gauge configuration with $Q = 1$.
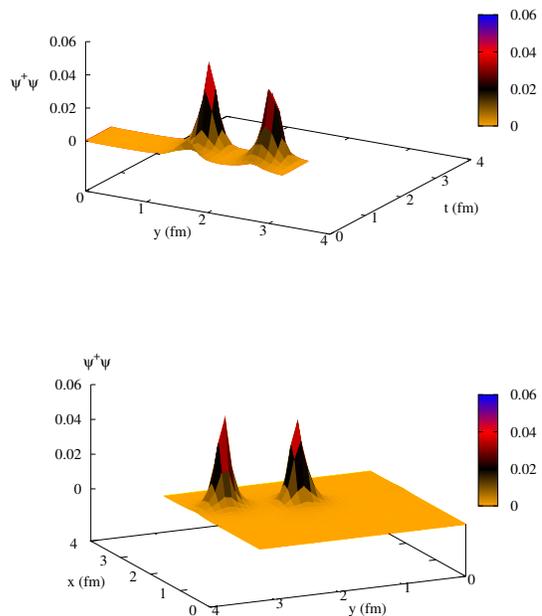


Fig. 13: Space-time profile of a near-zero mode at $1.5\,T_c$ for the same gauge configuration depicted in Fig. 12.

When the instanton size is much smaller than $1/T$, the copies do not feel the effect of the neighbors and behave like zero temperature instantons. However, the overlap between the instanton copies may be larger and their sizes become comparable to $1/T$. Explicit solutions are known for trivial [54] as well as nontrivial [55, 56] holonomy. In the case of trivial holonomy it has been observed that the caloron turns into a magnetic monopole [57] in pure gauge theory. Calorons with nontrivial holonomy have more interesting features with monopole substructures [58]. However, in our studies we have not attempted to take a detailed look at the monopoles.

In order to gain more inside into the structure of the infrared modes in QCD, we looked at the profiles of the zero and the near-zero modes at $1.5\,T_c$. Examples representing the majority of configurations with topological charge $|Q| = 1$ are shown in Figs. 12 and 13. In these figures the density of the wavefunctions, $\psi^\dagger(x)\psi(x)$, is measured along two spacetime directions, summing over the other two directions and the internal degrees of freedom (color and spin). We observe that the zero modes are localized along the spatial as well as the temporal directions. In a few cases, the width of the zero modes in the compact temporal direction is somewhat larger and the density profile represents the overlap between the nearest copies.

The near-zero modes typically exhibit a two-peak structure, in the density as well as in the chirality

$(\psi^\dagger(x)\gamma_5\psi(x))$ profile, cf. Fig. 14. In the latter case, the chirality contained in the two peaks is of opposite sign. These profiles provide a strong hint toward a picture where two zero modes with equal and opposite chiralities interact weakly, becoming a pair of near-zero modes when properly superposed.

The fermion zero mode $\psi_0(x)$ associated with an instanton is known analytically [19], giving a density of the form

$$\psi_0^\dagger(x)\psi_0(x) = \frac{2\rho^2}{\pi^2(x^2 + \rho^2)^3} \; , \qquad (11)$$

where $\rho$ is the radius of the instanton. When three of the spacetime coordinates are integrated over, the density along the remaining fourth coordinate, say $y$, becomes

$$f_y(y) = \frac{\rho^2}{2(y^2 + \rho^2)^{3/2}} \; . \qquad (12)$$

An estimate of the instanton size $\rho$ can be obtained by either finding the distance where this integrated density falls below $1/\sqrt{8}$ of its maximal value or by fitting Eq. (12) to the measured density. When estimating the size in the temporal direction, the second approach has the advantage that it can also accommodate cases where the size of the instanton $\sim 1/T$ and the periodic copies in the temporal direction have noticeable
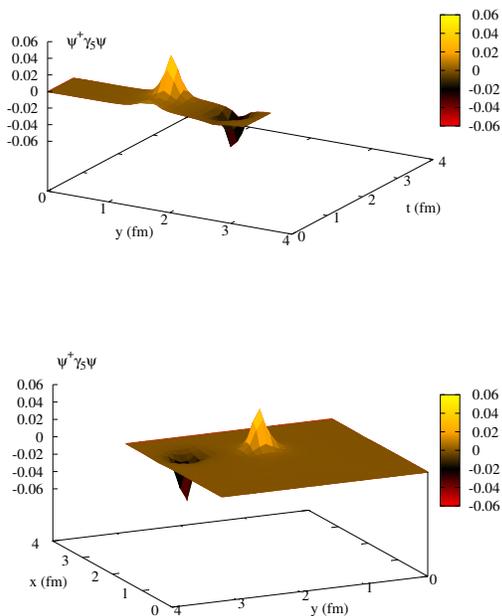
Fig. 14: Space-time profile of chirality of the same near-zero mode depicted in Fig. 13 at $1.5\,T_c$.



Fig. 15: Distribution of distances between the instanton and antiinstanton that couple to give rise to a near-zero mode. The blue points show the expected distribution if the instanton and antiinstanton were to be distributed randomly and independently of each other on a $32^3 \times 8$ lattice.



Fig. 16: Configuration distribution of the total number $n$ of zero and near-zero modes at $1.5\,T_c$ and Poisson fit to the data.

overlap. This is achieved by replacing the fit function by $\sum_{k=-n}^{n} f_\tau(\tau + k/T)$.

At $1.5\,T_c$, we measured the wavefunction density of the zero modes along each coordinate direction for all configurations with $|Q| = 1$ by summing over the other three directions. The radii of the profiles along the $x$, $y$ and $z$ directions, $\rho_x$, $\rho_y$ and $\rho_z$, were averaged over to give a spatial radius of $\rho_\sigma = 0.223(8)$ fm, essentially independent of which method was used. Along the temporal direction, using the adjusted fit ansatz we obtained a radius that was only slightly larger, namely $\rho_\tau = 0.24(1)$ fm.

In order to study the distribution of the distance between the instanton and antiinstanton forming a pair, the lattice points with the lowest and highest chiral density of the corresponding near-zero modes were identified and the distance between them was measured. The result is shown in Fig. 15. We compare this with the expected distribution of the separation if an instanton and an antiinstanton were to be distributed on the lattice randomly, independent of each other. It can be seen that the measured distribution compares quite well with the random distribution with a slight excess at small separations, further supporting the picture that instantons and antiinstantons are weakly interacting.

In a weakly interacting random ensemble of such topological objects, the assumption of independent occurrence results in a Poisson distribution for the total number $n$ of instantons and antiinstantons,

$$P_\kappa(n) = e^{-\kappa} \kappa^n / n!\,, \qquad (13)$$

where $\kappa$ is a parameter that is equal to the ensemble average $\langle n \rangle$ as well as the variance $\sigma^2$ and $n$ is obtained by counting the number of eigenvalues below a cutoff $\lambda_0$. To fix the cutoff, we fitted Eq. (13) to the distribution of $n$ for different cutoffs and compared the $\chi^2$ per degree of freedom. The value that was closest to 1, namely 1.03, was obtained for $\lambda_0 = 0.44\,T$. The resulting distribution is shown in Fig. 16 together with the Poisson fit which gives $\kappa = 4.5(2)$. At this cutoff, we obtained $\langle n \rangle = 4.50(14)$ and $\sigma^2 = 4.2(4)$ from averaging over the configurations, confirming that instantons and antiinstantons indeed occur almost independently.

Taking $4.5(2)$ as the average total number of instantons and antiinstantons per configuration, we obtain a density of $0.147(7)\,\mathrm{fm}^{-4}$, which is much lower than the value predicted from the strongly interacting dense ILM, $1\,\mathrm{fm}^{-4}$ [22]. However, since we are at a temperature much higher than the chiral crossover temperature $T_c$, it is not surprising that we get values expected rather from a dilute and weakly interacting ensemble.
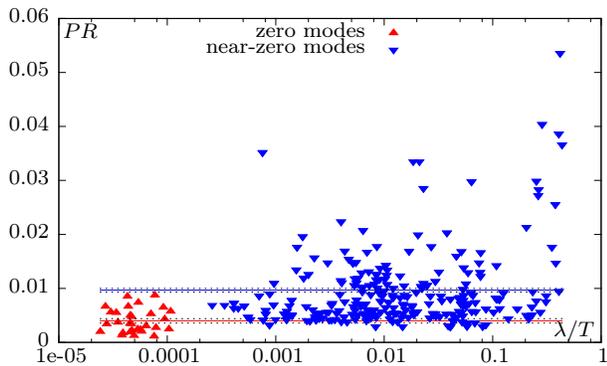
Fig. 17: Participation ratio of zero modes of $|Q| = 1$ configurations and near-zero modes ($\lambda/T < 0.4$) as well as their average values as function of the eigenvalue $\lambda$ at $T \sim 1.5\,T_c$.

Altogether, the findings described in this section are giving support to a picture in which for sufficiently high temperatures of $T \gtrsim 1.5\,T_c$, the infrared behavior of QCD can be described as that of a dilute gas of instantons and antiinstantons which are interacting weakly with each other.

## G.   The localization properties of the eigenmodes

The profiles of the near-zero modes have suggested that these are localized structures. To further quantify their localization properties and those of the bulk modes, we study the so-called participation ratio (PR), defined for a normalized eigenvector $\psi(x)$ of the Dirac operator as

$$PR = \frac{1}{N_\sigma^3 N_\tau} \left[ \sum_x \left( \psi^\dagger(x)\psi(x) \right)^2 \right]^{-1} . \qquad (14)$$

It is the fraction of the total lattice volume occupied by the eigenmode. If the eigenvector is distributed equally on the entire four-volume, this quantity is unity.

First we use the PR to corroborate our observation made in Sec. III F. If indeed the near-zero modes represent weakly interacting instanton-antiinstanton pairs, the PR of a typical near-zero mode should be about twice as large as that of a zero mode. The comparison of the PR of the near-zero modes and of the zero modes of $|Q| = 1$ configurations is shown in Fig. 17. The ratio of the average PR of a near-zero and that of a zero mode indeed is 1.85. The PR values of near-zero modes fluctuate about the mean value, so not all of them support this picture, but there is a significant fraction that does.

At $1.2\,T_c$, the PR histograms are measured for two values of the lattice spacing and compiled in Fig. 18. The low-lying eigenvalues are more localized than the bulk modes; however, the PR gradually increases as one goes towards the bulk. At $1.5\,T_c$, the low-lying modes below $\lambda \leq 0.4\,T$ average to a PR value of about 0.01. As one enters the bulk eigenvalue region for $\lambda > 0.4\,T$, see for
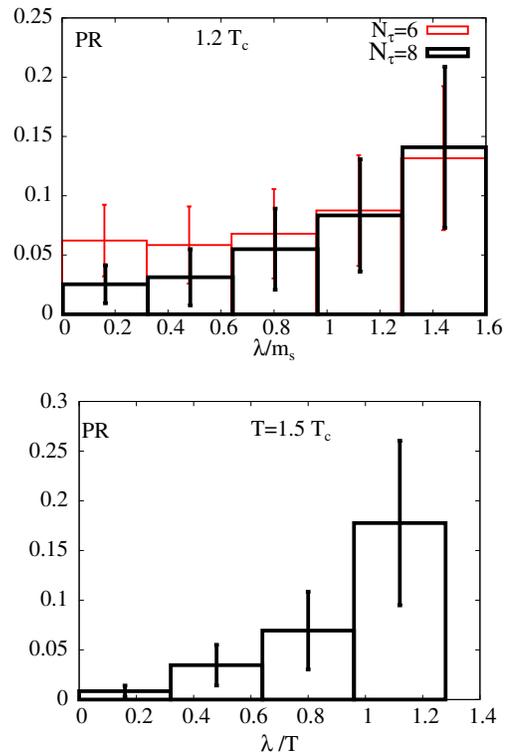




Fig. 18: The PR for eigenvectors at 1.2 and 1.5 $T_c$. The 1.2 $T_c$ data are for two different lattice spacings to study the cutoff dependence of our results.

example Fig. 9, there appears to be a rise of the PR. The value of $\lambda \approx 0.4\,T$ may thus be considered as a mobility edge separating the localized near-zero eigenstates from the delocalized bulk states. However it would further require careful finite volume analysis to check whether this will survive in the thermodynamic limit. The presence of localized as well as delocalized states is observed in disordered semiconductors whose dynamics is described by the Anderson Hamiltonian. In the Anderson model, the electron states at the band edge are localized whereas the states at the band center remain delocalized within the lattice. The corresponding eigenvalues of the Anderson Hamiltonian change from Poisson statistics at the band edge to random matrix theory statistics at the band center.

A comparison with random matrix model predictions can be achieved by looking at the distribution of the distance $s$ between two consecutive eigenvalues, i.e. the level spacing distribution. In order to understand its universal properties, it is necessary to map the eigenvalues onto new values using an unfolding procedure [59], thereby removing the non-universal global scale of the system. By construction, the unfolded eigenvalues that are obtained by this method have a mean level spacing of unity.

While the unfolded level spacings of the localized near-zero modes should follow a Poisson distribution because of their mostly independent occurrence, the bulk
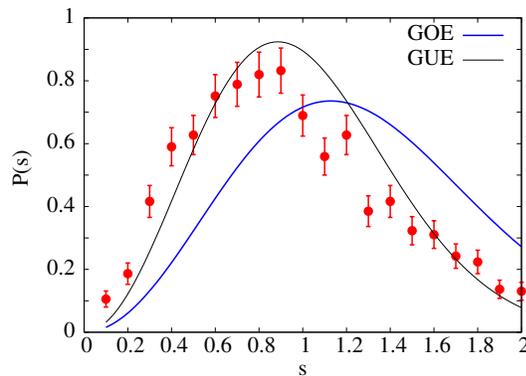
Fig. 19: The universal level spacing distribution for $\lambda > 0.4\,T$ at $1.5\,T_c$ compared to the Random Matrix theory Gaussian Unitary ensemble (GUE) and the Gaussian Orthogonal ensemble (GOE).

modes should be strongly mixed. If the bulk is highly disordered, the corresponding level spacing distribution should follow the same distribution as the eigenvalues of a random matrix of an appropriate symmetry group. The Dirac operator for QCD with matter fields in the fundamental representation falls into the same symmetry group as Gaussian Unitary ensembles (GUE) whereas for the case of two colors it is in the same universality class as Gaussian Orthogonal ensembles (GOE). The level spacing distribution for the unfolded bulk eigenvalues of the overlap operator on HISQ configurations at $1.5\,T_c$ is shown in Fig. 19. It shows an agreement with a random matrix theory with Gaussian unitary matrices. This is in general agreement with similar studies of the localization of low-lying modes done before for the quenched theory [21, 61–63] and also with dynamical staggered fermions [60, 64, 65] on smaller lattice sizes.

## IV.   CONCLUSIONS

In this work we have investigated the temperature dependence of the anomalous $U_A(1)$ symmetry breaking in the high temperature phase of QCD with two light quark flavors. To this end we have employed the overlap Dirac operator exploiting its property of preserving the index theorem even at nonvanishing lattice spacing. We have applied the overlap operator on large volume HISQ gauge field configurations and computed its low-lying eigenmodes. We observe the presence of zero as well as near-zero modes in the investigated temperature range of $T_c \lesssim T \lesssim 1.5\,T_c$. By comparing the low-lying eigenmodes from two lattice spacings and studying the

effects of smearing we have shown that these infrared modes are not mere lattice cutoff effects.

We mainly analyzed configurations which have been obtained at a light sea quark mass corresponding to a pion mass of 160 MeV. However, within the set of configurations at our disposal, at a temperature near $T_c$ we could confirm the accumulation of the near zero eigenvalues also at a quark mass considerably below its physical value.

By quantifying the contribution of the near-zero eigenmodes to a specific combination of two point correlation functions, $\chi_\pi - \chi_\delta$, we conclude that these modes are primarily responsible for the anomalous breaking of the axial symmetry in QCD still being visible for $T_c \lesssim T \lesssim 1.5\,T_c$. Through detailed studies of their spacetime profiles, localization properties and distributions over gauge configurations we have shown that for $T \sim 1.5\,T_c$ the near-zero modes follow the behavior as expected of a gas of widely separated, weakly interacting instantons and antiinstantons. At $1.5\,T_c$ we find the density of (anti)instantons to be $0.147(7)\,\mathrm{fm}^{-4}$, with a typical radius of $0.223(8)$ fm. At this temperature, the spatial volume of our lattice was $\sim (3.3\,\mathrm{fm})^3$ with $1/T \sim 0.83$ fm, suggesting that the instanton gas is indeed dilute, the instanton size is smaller than $1/T$ and our chosen volume being large enough to accommodate more that one instanton–antiinstanton pair on average. In conclusion, our study suggests that at $T \sim 1.5\,T_c$ the origin of global $U_A(1)$ breaking in QCD is due to the dilute gas of weakly interacting instantons and antiinstantons.

For an independent confirmation of our results, it would clearly be desirable to carry out a similar analysis with dynamical chiral fermions. While the lattice spacing effects in this work appear to be small, it will further be necessary to control the subtle extrapolations to the continuum as well as the chiral limit in such a future investigation.

[1] C. Bernard et. al., Phys. Rev. D 71, 034504 (2005).

[2] M. Cheng et. al., Phys. Rev. D 74, 054507 (2006).

[3] Y. Aoki et. al., Nature 443, 675678 (2006).

[4] T. Bhattacharya et. al., Phys. Rev. Lett. 113, 082001 (2014).

[5] A. Bazavov et. al., Phys. Rev. D 85, 054503 (2012).

[6] S. L. Adler, Phys. Rev. 177, 2426 (1969).
J. Bell and R. Jackiw, Nuovo. Cim. A 60, 47 (1969).

[7] K. Fujikawa, Phys. Rev. Lett. 42, 1195 (1979).

[8] G. 't Hooft, Phys. Rev. Lett. 37, 8 (1976).

[9] R. D. Pisarski and F. Wilczek, Phys. Rev. D 29, 338 (1984).

[10] A. Butti, A. Pelissetto, E. Vicari, JHEP 0308, 029 (2003).

[11] A. Pelissetto and E. Vicari, Phys. Rev. D 88, 105018 (2013).

[12] M. Grahl and D. H. Rischke, Phys. Rev. D 88, 056014 (2013).

[13] T. Sato and N. Yamada, Phys. Rev. D 91, 034025 (2015).

[14] Y. Nakayama and T. Ohtsuki, Phys. Rev. D 91, 021901 (2015).

[15] E. Shuryak, Comments Nucl. Part. Phys. 21, 235 (1994).

[16] T. Banks and A. Casher, Nucl. Phys. B 169, 103 (1980).

[17] S. Aoki, H. Fukaya, Y. Taniguchi, Phys. Rev. D 86, 114512 (2012).

[18] A. Bazavov et. al. Phys. Rev. D 86, 094503 (2012).

[19] G. t'Hooft, Phys. Rev. D 14, 3432 (1976).

[20] D. J. Gross, R. D. Pisarski and L. G. Yaffe, Rev. Mod. Phys. 53, 43 (1981).

[21] R. G. Edwards, U. M. Heller, J. Kiskis and R. Narayanan, Phys. Rev. D 61, 074504 (2000).

[22] E. V. Shuryak, Nucl. Phys. B 203, 93 (1982).

[23] E. -M. Ilgenfritz and E. V. Shuryak Nucl. Phys. B 319, 511 (1989).

[24] T. Schaefer, E. Shuryak and J. J. M. Verbaarschot, Phys. Rev. D 51, 1267 (1995).

[25] E. -M. Ilgenfritz and E. V. Shuryak, Phys. Lett. B 325, 263 (1994).

[26] T. Kanazawa and N. Yamamoto, arxiv:1410.3614 [hep-th].

[27] S. Chandrasekharan and N. H. Christ, Nucl. Phys. Proc. Suppl. 47, 527 (1996).

[28] M. Cheng et. al., Eur. Phys. J. C 71, 1564 (2011).

[29] B. Brandt et. al., PoS LATTICE2013, 162 (2014).

[30] E. Follana et al. (HPQCD Collaboration and UKQCD Collaboration), Phys. Rev. D 75, 054502 (2007).

[31] H. Ohno, U. M. Heller, F. Karsch and S. Mukherjee, PoS LATTICE 2011, 210 (2011); PoS LATTICE 2012, 095 (2012).

[32] D. H. Adams, Phys. Rev. Lett. 104, 141602 (2010).

[33] M. I. Buchoff et. al., Phys. Rev. D 89, 054514 (2014).

[34] T. W. Chiu et. al., PoS LATTICE2013 165 (2014).

[35] G. Cossu et. al., Phys. Rev. D 87, 114514 (2013).

[36] G. Cossu et. al. (JLQCD collaboration) arxiv:1412.5703 [hep-lat].

[37] Ph. de Forcrand, M. Garcia Perez and I.-O. Stamatescu, Nucl. Phys. Proc. Suppl. 53, 557 (1997).

[38] T. DeGrand, A. Hasenfratz, and T. G. Kovacs, Nucl. Phys. B 520, 301 (1998).

[39] A. Hasenfratz and F. Knechtli, Phys. Rev. D 64, 034504 (2002).

[40] M. Atiyah and I. Singer, Bull. Amer. Math. Soc, 69 (3) 422 (1963).

[41] A. Bazavov et. al. [HotQCD Collaboration], Phys. Rev. D 90, 094503 (2014).

[42] H.-T. Ding et. al., PoS LATTICE 2013, 157 (2014).

[43] R. Narayanan and H. Neuberger, Phys. Rev. Lett. 71, 3251 (1993);
H. Neuberger, Phys. Lett. B 417, 141 (1998).

[44] S. B. Nielsen and M. Ninomiya, Nucl. Phys. B 185, 20 (1981).

[45] P. Hasenfratz, V. Laliena and F. Niedermeyer, Phys. Lett. B 427, 125 (1998).

[46] D. H. Adams, Annals Phys. 296, 131 (2002).

[47] R. V. Gavai, S. Gupta and R. Lacaze, Phys. Rev. D 65, 094504 (2002).

[48] S. Sharma et. al., PoS LATTICE 2013, 164 (2014).

[49] T. Kalkreuter and H. Simma, Comput. Phys. Commun. 93, 33 (1996).

[50] A. Hasenfratz, R. Hoffmann, S. Schaefer, JHEP 0711, 071 (2007).

[51] A. V. Smilga and J. Stern, Phys. Lett. B 318, 531 (1993).

[52] J. J. M. Verbaarschot, Nucl. Phys. B 427, 534 (1994).

[53] C. Bernard, C. E. DeTar, Z. Fu and S. Prelovsek, Phys. Rev. D 76, 094504 (2007).

[54] B. J. Harrington and H. K. Shepard, Phys. Rev. D 17, 2122 (1978).

[55] T. Kraan and P. van Baal, Nucl. Phys. B 533, 627 (1998).

[56] K. -M. Lee and C. -H. Lu, Phys. Rev. D 58, 025011 (1998).

[57] P. Rossi, Nucl. Phys. B 149, 170 (1979).

[58] V. Bornyakov, E. -M. Ilgenfritz, B. Martemyanov, V. Mitrjushkin and M. Mueller-Preussker, Phys. Rev. D 87, 114508 (2013).

[59] T. Guhr, A. Mueller-Groeling and H. A. Weidenmueller, Phys. Rept. 299, 189 (1998).

[60] A. M. Garcia-Garcia and J. Osborn, Phys. Rev. D 75, 034503 (2007).

[61] R. Gavai and S. Gupta, Phys. Rev. D 65, 094504 (2002).

[62] T. G. Kovacs, Phys. Rev. Lett. 104, 031601 (2010).

[63] T. G. Kovacs and F. Pittler, Phys. Rev. Lett. 105, 192001 (2010).

[64] R. Gavai and S. Gupta, Phys. Rev. D 77, 114506 (2008).

[65] M. Giordano, T. G. Kovacs, F. Pittler, Phys. Rev. Lett. 112, 102002 (2014).

[66] M. A. Clark et. al., Comput. Phys. Commun. 181, 1517 (2010).